Transient rheology of the upper mantle beneath central Alaska inferred from the crustal velocity field following the 2002 Denali earthquake

Fred F. Pollitz

U.S. Geological Survey, Menlo Park, California

Short title: POST-DENALI EARTHQUAKE DEFORMATION

Abstract. The M7.9 2002 Denali earthquake, Alaska, is one of the largest strike-slip earthquakes ever recorded. The postseismic GPS velocity field around the 300-km long rupture is characterized by very rapid horizontal velocity up to $\sim$ 300 mm/yr for the first 0.1 years and slower but still elevated horizontal velocity up to $\sim$ 100 mm/yr for the succeeding 1.5 years. I find that the spatial and temporal pattern of the displacement field may be explained by a transient mantle rheology. Representing the regional upper mantle as a Burghers body, I infer steady state and transient viscosities of $\eta_1 = 2.8 \times 10^{18}$ Pa s and $\eta_2 = 1.0 \times 10^{17}$ Pa s, respectively, corresponding to material relaxation times of 1.3 years and 0.05 years. The lower crustal viscosity is poorly constrained by the considered horizontal velocity field, and the quoted mantle viscosities assume a steady state lower crust viscosity that is $7 \times \eta_1$. Systematic bias in predicted versus observed velocity vectors with respect to a fixed North America during the first 3 to 6 months following the earthquake is reduced when all velocity vectors are referred to a fixed site (DNLC). This suggests that the post-Denali GPS time series for the first 1.63 years are shaped by a combination of a common mode noise source during the first 3 to 6 months plus viscoelastic relaxation controlled by a transient mantle rheology.

1. Introduction

The M7.9 November 3, 2002 Denali earthquake, Alaska is the largest earthquake to have struck continental North America since 1857, and its seismic moment is at the upper limit of those ever produced by a strike-slip event [*Romanowicz and Ruff*, 2002]. With an overall rupture length of 300 km over the Denali and Totschunda faults (Figure 1) and average and maximum slips of 2.1 m and 10.3 m, respectively [*Dreger et al.*, 2004], it produced large static displacements at $\gtrsim$ 100 km distance [*Hreinsdóttir et al.*, 2003] and correspondingly large stress changes in the crust and upper mantle. These stress changes far exceed those produced by the M7.4 1992 Landers and M7.1 1999 Hector Mine earthquakes, California, both of which were associated with large postseismic crustal movements as constrained by Global Positioning System (GPS) data [e.g., *Shen et al.*, 1994; *Savage and Svarc*, 1997; *Owen et al.*, 2002; *Hudnut et al.*, 2002] and InSAR data [*Peltzer et al.*, 1998; *Pollitz et al.*, 2001; *Fialko*, 2004].

The temporally-decaying postseismic movements after the Landers and Hector Mine earthquakes provided great insight into the rheology of the subsurface and the mechanics of postseismic deformation. Proposed mechanisms include afterslip [*Shen et al.*, 1994; *Savage and Svarc*, 1997; *Owen et al.*, 2002; *Hudnut et al.*, 2002], poroelastic rebound [*Peltzer et al.*, 1998; *Fialko*, 2004], and viscoelastic relaxation of the lower crust [*Deng et al.*, 1998] or upper mantle [*Pollitz et al.*, 2000; *Pollitz et al.*, 2001; *Freed and Bürgmann*, 2004]. The postseismic deformation field after both earthquakes was characterized by a very rapid transient for $\sim$ 1 month followed by a slower transient for

2 - 3 years elevated above background strain rates. Proposed origins for this behavior are a nonlinear rheology [*Pollitz et al.*, 2001; *Freed and Bürgmann*, 2004] and a transient rheology [*Pollitz*, 2003] represented by a Burghers body. Poroelastic rebound would also be expected to operate on a short time scale [*Jónsson et al.*, 2003] and likely influenced at least the short-term post-Landers movements [*Fialko*, 2004]. The studies of viscoelastic relaxation conclude that the dominant relaxation effect takes place in the upper mantle based on consideration of both horizontal and vertical postseismic movements.

The purpose of this study is to interpret GPS measurements of postseismic deformation in south-central Alaska for the first 19 months after the 2002 Denali earthquake. It has been noted that the time series from GPS sites near the Denali rupture exhibit two time scales of $\sim$ 1 month and 1.5 years [*Svarc and Savage*, 2004]. The GPS measurements may be satisfactorily explained by viscoelastic relaxation of the lower crust and upper mantle, the mantle rheology being governed by a transient rheology and dominating the overall relaxation process.

2. Data Set

We utilize a combination of campaign GPS data collected by the U.S. Geological Survey (USGS) and continuous GPS data that is part of the Alaska Deformation Array (AKDA). Station locations are shown in Figure 1. Representative time series from seven sites are shown in Figure 2. The USGS campaign data was collected in several surveys at four sites since the earthquake. The AKDA continuous data is available at eleven

sites that were installed within one week of the earthquake [*Freymueller et al.*, 2003]. Both data sets were processed simultaneously at the USGS using the GIPSY/OASIS II software [*Zumberge et al.*, 1997]. Time series are provided in a fixed North America reference frame based on ITRF2000 [*Altamimi et al.*, 2002]. They are re-sampled at 1 day intervals and made available on the world wide web (http://quake.wr.usgs.gov/research/deformation/gps/auto/Denali/).

Standard errors in individual measurements plotted in Figure 2 are approximately 4 mm for the horizontal components and 12 mm for the vertical components. No adjustment for a possible seasonal signal has been performed on the plotted data. The scatter may be reduced, however, by referring the time series to a fixed site. For example, the same time series in Figures 2a,b are shown with respect to a fixed DNLC in Figures 2c,d. The scatter in measurements is substantially reduced for all components, suggesting a common source of noise present in the most of the GPS measurements. Because of the great scatter in the vertical measurements, attention will be restricted to the horizontal time series.

3. Interpretation of Post-Denali Deformation

3.1. Temporal Pattern of the Deformation Field

Figure 2 demonstrates that horizontal postseismic displacements are shaped by a rapid transient for the first $\sim$ 0.1 years (Figure 2a,c) followed by a slower transient for the remaining 18 months (Figure 2b,d). Horizontal displacement rates are of order

100 mm/yr and 40 mm/yr for the first 0.1 years and last 0.5 years (i.e., 1.1 - 1.6 years following the earthquake), respectively. Even FAIR, which is $\sim$ 200 km distant from the Denali earthquake rupture, exhibits a rapid transient of $\sim$ 50 mm/yr for the first 0.1 years. This suggests that the underlying process driving the postseismic crustal deformation must be operating at depth well below coseismic rupture surface and involve 10s of km of the upper mantle. Interseismic deformation in this region is expected to be small, no more than $\sim$ 10 mm/yr, based on a model of strain accumulation along the Aleutian trench derived from pre-Denali GPS data [*Savage et al.*, 1999; *Freymueller et al.*, 2000]. Thus the relatively rapid deformation observed in the 19 months following the Denali earthquake is unique to the postseismic epoch.

3.2. Burghers Body Rheology

I choose a model of transient rheology to explain the horizontal postseismic observations. Transient rheology is here represented with a Burghers body [e.g., *Peltier and Yuen*, 1981] (Figure 3). The Burghers body is described by five parameters instead of the three needed to specify a Maxwell rheology. The two additional parameters are those in the Kelvin element: transient shear modulus μ_2 and transient viscosity η_2. It reduces to a Maxwell rheology if $\eta_2 = \infty$ or $\mu_2 = \infty$ (Figure 3). Since $\eta_1 \gg \eta_2$, the Maxwell and Kelvin elements are analogs for viscous and anelastic deformation processes, respectively. The Kelvin element is presumably one component of a continuum in an absorption band model of seismic wave attenuation [e.g., *Anderson and Given*, 1982; *Yuen and Peltier*, 1982].

The regional model is parameterized in Figure 4 and consists of an elastic upper crust underlain by a Maxwell viscoelastic lower crust and Burghers body upper mantle. The spherically-layered model has an outer radius of 6371 km. For simplicity the lower crust and mantle are assumed to be homogeneous and of constant thickness. The base of the lower crust is assigned a depth of 38 km based on the average depth of the regional Moho [*Ferris et al.*, 2003]. The mantle is unbounded in depth, i.e., it is idealized as a homogeneous viscoelastic sphere of radius 6333 km.

3.3. Determination of Rheology Parameters

Predicted postseismic deformation depends on a specified viscoelastic model and dislocation sources for the earthquake. We use the Denali earthquake coseismic rupture model of *Dreger et al.* [2004] for this purpose. Postseismic displacements are then calculated using the method of [*Pollitz*, 1997], modified to the case of a Burghers body rheology using the transformed shear modulus appropriate for that material [*Pollitz*, 2003].

The elastic parameters are known from seismic information, leaving four unknown viscoelastic parameters: lower crust viscosity η_c, steady state upper mantle viscosity η_1, transient viscosity η_2, and transient shear modulus μ_2. We explore three classes of models:

M1: $\eta_c/\eta_1 = 7$, $\mu_2 = \mu_1$, η_1 and η_2 variable (biviscous upper mantle)

M2: $\eta_c/\eta_1 = 1$, $\mu_2 = \mu_1$, η_1 and η_2 variable (biviscous upper mantle)

M3: $\eta_c/\eta_1 = 7$, $\eta_2 = \infty$, η_1 variable (Maxwell rheology model)

Following *Pollitz* [2003] we perform a grid search over the variable parameters using postseismic velocity within selected time windows. This was found by *Pollitz* [2003] to be a more robust procedure than fitting the set of time series directly because unmodeled processes (e.g., laterally heterogeneous rheology) tend to cause modeled displacement-time series curves to drift from observed displacements for many of the time series, in which case misfits of later portions of the time series would dominate the model fits. Because most time series do not begin immediately after the earthquake (i.e., at time zero in Figure 2) and because the measurements contain errors, *Pollitz* [2003] introduced a set of initial site positions $\{a_i\}$ (each associated with time series $\#i$) plus a single three-component velocity shift vector $\mathbf{b}$ when evaluating one realization of a viscoelastic model. For example, for Model M1 with given values of η_1 and η_2, the set of observed time series is optimally fit to the set of calculated time series by deriving the $\{a_i\}$ and $\mathbf{b}$ in a least squares inversion. The resulting fit to the observations is then represented by the χ^2 misfit to postseismic velocity within selected time windows (equation 10 of *Pollitz* [2003]). We follow the same approach here except that $\mathbf{b}$ is fixed at zero. Inversions in which variable $\mathbf{b}$ are included tend to yield $\mid \mathbf{b} \mid \sim 30$ mm/yr, which is small compared with the signal but much larger than the pre-earthquake motion of this region with respect to fixed North America which likely did not exceed 10 mm/yr.

Figures 5a and 5b show the results of a grid search over η_1 and η_2 for Models M1 and M2, respectively, in terms of the misfit of velocity with respect to fixed North America within four different time periods. The black circles in these plots indicate

the combination of η_1 and η_2 judged to best fit all time periods simultaneously. The corresponding viscoelastic parameters are listed in Table 1. Fits of these models to the observed time series are shown in Figure 2 (red curves for M1, green curves for M2). Corresponding observed and predicted horizontal velocity vectors in various time periods are shown in Figure 6. Both Models M1 and M2 capture the rapid early transient and slower later transient, and it is difficult to distinguish these two models on the basis of the horizontal time series alone.

4. Discussion

A linear Maxwell rheology for the lower crust and mantle is prescribed by Model M3. If this rheology is calibrated to fit the later (post-3 months) part of the time series then we obtain $\eta_1 = 2.8 \times 10^{18}$ Pa s. The fit of this model to the observed time series is given by the blue curves in Figure 2. It clearly fails to capture the rapid transient exhibited at all sites during the first 3 months (Figures 2a,c). The predicted velocity field is satisfactory after 3 months (Figure 6c) but not for time intervals involving earlier times. This result is found to be similar for various assigned ratios η_c/η_1 (Model 3 assumes a ratio of 7). This demonstrates that viscoelastic relaxation governed by a linear Maxwell rheology cannot explain the horizontal postseismic deformation pattern observed for the 19 months after the Denali earthquake, at least if the assumption of homogeneous structure of the lower crust and upper mantle is correct.

Although it is difficult to discriminate between Models M1 and M2 and hence constrain lower crust viscosity, the postseismic velocity of the most distant site (FAIR)

may place a constraint on the depth extent of the anelastic component of the rheology. The predicted southward velocity of FAIR is greater than observed during the first 3 to 6 months postseismic time interval, and this suggests a slight revision to the anelastic component of the rheology. We investigate this possibility by modifying model M1 to have $\mu_2 = \infty$ at depth >138 km, all other properties being unchanged. The postseismic velocity field for the case $\eta_1 = 2.8 \times 10^{18}$ Pa s, $\eta_2 = 1.0 \times 10^{17}$ Pa s is shown in Figure 6d. This provides as good a fit to the postseismic velocities at near-fault sites and fits postseismic velocity at FAIR somewhat better during the first 3 to 6 months. This explanation is of course neither unique nor entirely sufficient.

The Burghers body model provides a modest fit to original post-Denali time series (i.e., those referred to a fixed North America in Figures 2a,b) in an average sense, but the model curves are shifted too high or too low for most time series. From the point of view of fitting the data, the present model has only four independent parameters (section 3.3). The preferred choice of these parameters tends to fit the slopes of the time series well, but imperfections in the model cause most predicted time series to drift up or down from observed time series. In addition to unmodelled processes, this may represent shortcomings of the Earth model, which is likely laterally heterogeneous and more complicated than a simple layered structure. The slip model of the Denali earthquake used here may have slight inaccuracies that could affect the predicted postseismic response. However, the slip models of *Hreinsdottir et al.* [2003] and *Dreger et al.* [2004] are similar. This together with the excellent fit of the 3 months - 1.63 years postseismic velocity pattern (Figure 6a,d) suggest that the source model is quite

accurate. Most likely, common mode noise in the observed time series adversely affects the fit of all models which are referred to a fixed North America. This is supported by the very good fit of model time series to observed time series referred to a fixed DNLC (i.e., red curves Figures 2c,d). In this comparison, one is fitting observed time series with a model of combined viscoelastic relaxation and a common mode noise source which is effectively removed by referring the GPS measurements to a fixed site. Referring the velocity vectors to a fixed DNLC (Figure 7) also shows that a common noice source could account for part of the bias in modeled velocity vectors during the early time periods ($\leq$ 3 to 6 months) where model velocity vectors have consistently smaller northward component than observed (e.g., Figures 6a,b,d)

I have not considered either afterslip or poroelastic rebound in this study. The large postseismic velocities exhibited at sites $\gtrsim$ 100 km distance from the Denali rupture (i.e., TLKA and FAIR) require a mantle source driving most of the postseismic deformation. This cannot be accomplished with a model of poroelastic rebound, which involves fluid flow in the shallow crust where permeability where permeability is sufficiently high [*Ingebritsen and Manning*, 1999] and affects only a region within a few km of the fault [*Jónsson et al.*, 2003]. A model of time-dependent deep afterslip could be constructed to fit the postseismic observations, as was done by *Bürgmann et al.* [2003] for the first year of post-Denali deformation. Such afterslip must penetrate to $\gtrsim$ 100 km depth in the mantle in order to adequately capture the large postseismic velocities of TLKA and FAIR. However, the high temperatures that likely exist in the central Alaska mantle [*Stachnik et al.*, 2004] favor bulk viscoelastic relaxation over plastic flow. Shallow

afterslip, however, may improve the fit of postseismic velocity at near-fault sites such as MENT, where the model predicted amplitude is considerably less than observed during the first three months (Figure 6a,d). Using a model of predominantly mantle viscoelastic relaxation, *Freed et al.* [2004] found that shallow afterslip on the Denali Fault near this site would improve its fit while leaving the fit at more distant sites unaffected.

It has been noted that virtually all continuous GPS time series following the 1999 Hector Mine and 2002 Denali earthquakes exhibit a $\log(1 + t/\tau)$ behavior [*Herring*, 2003; *Savage*, 2005], where $\tau \sim$ one day. Remarkably, these authors find that a combination of linear and logaithmic functions of time fits most time series well over a broad range of times $\sim 10^{-3}$ to $\sim 10^{-1/2}$ years. *Perfettini and Avouac* [2004] obtain good fits with the logarithmic function out to 200 days following the 1999 Chi-Chi earthquake. A sum of two decaying exponential functions with appropriate choice of weights behaves mathematically similar to a $\log(1 + t/\tau)$ function at short to intermediate times. The Burghers body model corresponds to a sum of two decaying exponentials for a constant stress step; it corresponds to a sum of several thousand decaying exponentials for general post-earthquake relaxation due to dispersion on a spherically layered Earth model as a function of spherical harmonic degree [*Pollitz*, 2003]. A $\log(1 + t/\tau)$ time dependence is precisely the Lomnitz creep function [*Lomnitz*, 1957], which describes low-temperature transient creep. This law should be combined with one of steady state creep in order to capture longer-term viscous deformation. The Burghers body model carries the advantage of containing the basic elements of both transient and steady state creep while mimicking the behavior of the Lomnitz creep function at short

times. Nevertheless, the Burghers body models constrained by post-earthquake GPS observations after the Hector Mine and Denali earthquakes detect only the longer end of the spectrum of relaxation times that likely characterize the full anelastic behavior of the mantle [e.g., *Anderson and Given*, 1982; *Yuen and Peltier*, 1982].

5. Conclusions

Horizontal postseismic crustal deformation as constrained by GPS in the 19 months following the 2002 Denali earthauake is explained as viscoelastic relaxation of the central Alaska lower crust and upper mantle. The GPS time series are characterized by a rapid transient up to $\sim$ 300 mm/yr over the first $\sim$ 0.1 years followed by a slower transient up to $\sim$ 100 mm/yr over the succeeding 18 months. These rates are well above the $\lesssim$ 10 mm/yr motions expected from background tectonic motions. The large postseismic velocities at sites more than 100 km distant from the Denali earthquake rupture, combined with the fact that two distinct time scales are exhibited in the GPS time series even at these distant sites, demands that a rheology with at least two material relaxation times characterize the central Alaska upper mantle. A transient rheology in the upper mantle adequately captures the two differing time scales. The material relaxation times of the upper mantle in the preferred model are 0.05 years and 1.3 years, being associated with the transient and steady state viscosities, respectively. Because only horizontal and not vertical deformation is considered, it is difficult to resolve lower crust viscosity. The transient rheology model advocated here is non-unique, and a non-linear (stress-dependent) rheology may be equally capable of explaining the considered GPS

time series. If a transient rheology is controlling post-Denali crustal deformation, then it suggests that the anelastic component of the complete rheology plays an important role in shaping the postseismic response of the crust and upper mantle after a large earthquake.

Acknowledgments. I am grateful to Jim Savage for numerous discussions and Jerry Svarc for advice with the GPS data. This work benefitted from internal reviews by Jim Savage and Ruth Harris and comments on a preliminary draft by Roland Bürgmann and Andy Freed.

References

Altamimi, Z., P. Sillard, and C. Boucher, ITRF2000: A new release of the International Terrestrial Reference Frame for earth science applications, *J. Geophys. Res.*, *107*, ETG2–1 – ETG2–19, 2002.

Anderson, D., and J. Given, Absorption band Q model for the earth, *J. Geophys. Res.*, *87*, 3893–3904, 1982.

Bürgmann, R., E. Calais, A. Freed, J. Freymueller, and S. Hreinsdóttir, Mechanics of Postseismic Deformation Following the 2002, Mw=7.9, Denali Fault Earthquake, *EOS Trans. AGU*, *84*, Fall Meet. Suppl., Abstract G21B–0270, 2003.

Deng, J., M. Gurnis, H. Kanamori, and E. Hauksson, Viscoelastic flow in the lower crust after the 1992 Landers, California, earthquake, *Science*, *282*, 1689–1692, 1998.

Dreger, D., D. Oglesby, R. Harris, N. Ratchkovski, and R. Hansen, Kinematic and dynamic rupture models of the November 3, 2002 Mw7.9 Denali, Alaska, earthquake, *Geophys. Res. Lett.*, *31*, 10.1029/2003GL018,333, 2004.

Ferris, A., G. Abers, D. Christensen, and E. Veenstra, High resolution image of the subducted Pacific (?) plate beneath central Alaska, 50-150 km depth, *Earth Planet. Sci. Lett.*, *214*, 575–588, 2003.

Fialko, Y., Evidence of fluid-filled upper crust from observations of post-seismic deformation due to the 1992 Mw7.3 Landers earthquake, *J. Geophys. Res.*, *109*, 10.1029/2003JB002,985, 2004.

Freed, A., and R. Bürgmann, Evidence of powerlaw flow in the Mojave desert mantle, *Nature*, *430*, 548–551, 2004.

Freed, A., J. Freymueller, H. Fletcher, S. Hreinsdóttir, C. Larsen, R. Bürgmann, and E. Calais, The Denali Fault: Crustal Deformation Before and After the 2002, Mw=7.9, Denali Fault Earthquake, *EOS Trans. AGU*, *84*, Fall Meet. Suppl., Abstract S11B–05, 2004.

Freymueller, J., S. Cohen, and H. Fletcher, Spatial variations in present-day deformation, Kenai Peninsula, Alaska, and their implications, *J. Geophys. Res.*, *105*, 8097–8101, 2000.

Freymueller, J., H. Fletcher, S. Hreinsdóttir, C. Larsen, R. Bürgmann, E. Calais, and A. Freed, The Denali Fault: Crustal Deformation Before and After the 2002, Mw=7.9, Denali Fault Earthquake, *EOS Trans. AGU*, *84*, Fall Meet. Suppl., Abstract S11B–05, 2003.

Herring, T., Results and comparisons from the Southern California Integrated and other arrays, *EOS Trans. AGU*, *84(46)*, Fall Meet. Suppl., Abstract G32B–04, 2003.

Hreinsdóttir, S., J. Freymueller, H. Fletcher, C. Larsen, and R. Bürgmann, Coseismic slip distribution of the 2002 Mw7.9 Denali fault earthquake, Alaska, determined from GPS measurements, *Geophys. Res. Lett.*, *30*, 1674, 10.1029/2003GL017,447, 2003.

Hudnut, K. W., et al., Continuous GPS observations of postseismic deformation following the 16 October 1999 Hector Mine earthquake (Mw7.1), *Bull. Seismol. Soc. Am.*, *92*, 1403–1422, 2002.

Ingebritsen, S., and C. Manning, Geological implications of a permeability-depth curve for the continental crust, *Geology*, *27*, 1107–1110, 1999.

Jónsson, S., P. Segall, R. Pedersen, and G. Björnsson, Post-earthquake ground movements correlated to pore-pressure transients, *Nature*, *424*, 179–183, 2003.

Lomnitz, C., Linear dissipation in solids, *J. Appl. Phys.*, *28*, 201–205, 1957.

Owen, S., G. Anderson, D. Agnew, H. Johnson, K. Hurst, R. Reilinger, Z.-K. Shen, J. Svarc, and T. Baker, Early postseismic deformation from the 16 October 1999 Mw 7.1 Hector Mine, California, earthquake as measured by Survey- Mode GPS, *Bull. Seismol. Soc. Am*, *92*, 1423–1432, 2002.

Peltier, W., P. Wu, and D. Yuen, The viscosities of the earths mantle, *Anelasticity in the Earth*, *American Geophysical Union Geodynamics Series (F.D. Stacey, A. Nicolas, M.S. Peterson, eds.)*, Washington, DC, 59–71, 1981.

Peltzer, G., P. Rosen, F. Rogez, and K. Hudnut, Post-seismic deformation along the Landers 1992 earthquake surface rupture, *J. Geophys. Res.*, *103*, 30,131–30,145, 1998.

Perfettini, H., and J.-P. Avouac, Postseismic relaxation driven by brittle creep: A possible mechanism to reconcile geodetic measurements and the decay rate of aftershocks, application to the Chi-Chi earthquake, Taiwan, *J. Geophys. Res.*, *109*, 10.1029/2003JB002,488, 2004.

Pollitz, F. F., Gravitational viscoelastic postseismic relaxation on a layered spherical earth, *J. Geophys. Res.*, *102*, 17,921–17,941, 1997.

Pollitz, F. F., Transient rheology of the uppermost mantle beneath the Mojave Desert, California, *Earth Planet. Sci. Lett.*, *215*, 89–104, 2003.

Pollitz, F. F., G. Peltzer, and R. Bürgmann, Mobility of the continental mantle : Evidence from postseismic geodetic observations following the 1992 Landers earthquake, *J. Geophys. Res.*, *105*, 8035–8054, 2000.

Pollitz, F. F., C. Wicks, and W. Thatcher, Mantle flow beneath a continental strike-slip

fault : Postseismic deformation after the 1999 Hector Mine earthquake, *Science*, *293*, 1814–1818, 2001.

Romanowicz, B., and L. Ruff, On moment-length scaling of large strike-slip earthquakes and the strength of faults, *Geophys. Res. Lett.*, *29*, 10.1029/2001GL014,479, 2002.

Savage, J., J. Svarc, and W. Prescott, Deformation across the Alaska-Aleutian subduction zone near Kodiak, *Geophys. Res. Lett.*, *26*, 2117–2120, 1999.

Savage, J. C., Postseismic relaxation and transient creep, *J. Geophys. Res.*, *in preparation*, 2005.

Savage, J. C., and J. Svarc, Postseismic deformation associated with the 1992 Mw=7.3 Landers earthqake, southern California, *J. Geophys. Res.*, *102*, 7565–7577, 1997.

Shen, Z.-K., D. Jackson, Y. Feng, M. Cline, M. Kim, P. Fang, and Y. Bock, Postseismic deformation following the Landers earthquake, California, *Bull. Seismol. Soc. Am.*, *84*, 780–791, 1994.

Stachnik, J., G. Abers, and D. Christensen, Seismic attenuation and mantle wedge temperatures in the Alaska subduction zone, *J. Geophys. Res.*, *109*, 10.1029/2004JB003,018, 2004.

Svarc, J., and J. Savage, Postseismic deformation measured with GPS immediately following the 2003 San Simeon earthquake, *Seismol. Res. Lett.*, *74*, 294, 2004.

Yuen, D., and W. Peltier, Normal modes of the viscoelastic Earth, *Geophys. J. Roy. Astr. Soc.*, *69*, 495–526, 1982.

Zumberge, J., M. Heflin, D. Jefferson, M. Watkins, and F. Webb, Precise point positioning for the efficient and robust analysis of GPS data from large networks, *J. Geophys. Res.*, *102*, 5005–5017, 1997.

F.F. Pollitz, U.S. Geological Survey, 345 Middlefield Rd., MS 977, Menlo Park, CA 94025. (e-mail: fpollitz@usgs.gov)

Received _____

Submitted to *Journal of Geophysical Research*, February 2005.

Figure 1. Background map indicating the faults that ruptured during the 2002 Denali earthquake. GPS sites used in this study are shown by triangles (USGS campaign sites) and circles (AKDA continuous sites). The fault segments used to model the Denali earthquake are shown in red.

Figure 2. Time series of selected USGS and AKDA GPS sites for the first 1.63 years (a) or first 0.25 years (b) following the 2002 Denali earthquake. Fits of these time series are indicated for three different models. Model M1, red curves: $\eta_1 = 2.8 \times 10^{18}$ Pa s, $\eta_2 = 1.0 \times 10^{17}$ Pa s. Model M2, green curves: $\eta_1 = 7.7 \times 10^{18}$ Pa s, $\eta_2 = 1.7 \times 10^{17}$ Pa s. Model M3, blue curves: $\eta_1 = 2.8 \times 10^{18}$ Pa s. Parts (c) and (d) display the same time series and model curves but referred to a fixed DNLC.

Figure 3. A transient rheology as represented by a Burghers body. It consists of a Maxwell element in series with a Kelvin element, which are characterized by steady state shear and bulk moduli μ_1 and κ_1, respectively, steady state viscosity η_1, transient viscosity η_2, and transient shear modulus μ_2. If $\eta_1 = \infty$, then the material behaves like a standard linear solid with relaxed shear modulus $\mu' = \mu_1\mu_2/(\mu_1 + \mu_2)$. If $\eta_2 = \infty$ or $\mu_2 = \infty$, then the material behavior reduces to a Maxwell rheology.

Figure 4. Layered Earth model for central Alaska used in this study. Based on a similar study [*Pollitz*, 2003] we assume a Maxwell and Burghers body rheology for the lower crust and upper mantle, respectively, and assume that relaxed shear modulus in the mantle $\mu' = 0.5 \times \mu_1$.

Figure 5. Residual misfit of a set of viscoelastic models with respect to observed velocities in four time periods. This is calculated from equation 10 of *Pollitz* [2003] for the horizontal velocity components (i.e., summed East and North components). (a) Misfit pattern for model M1. (b) Misfit pattern for Model M2. Parameters used for M1 and M2 are given in Table 1. Black circles indicate the viscosity combination that is subjectively judged to provide the best fit to each of the models.

Figure 6. Comparison of observed and calculated velocity fields for (a) Model M1, (b) M2, (c) M3, and (d) modified Model M1 (see text) for four different time periods after the Denali earthquake. Parameters used for M1, M2, and M3 are given in Table 1. The observed velocity field is referred to a fixed North America, and the calculated velocity field is referred to the inertial reference frame.

Figure 7. Comparison of observed and calculated velocity fields for Model M1 for four different time periods after the Denali earthquake. The observed and calculated velocity fields are identical to those in Figure 6a but are referred to a fixed DNLC.

Table 1. Parameters of Best-Fitting Viscoelastic Models

Model	Steady State Viscosity η_1 Pa s	Transient Viscosity η_2 Pa s	Steady State Viscosity η_c Pa s	Steady State Shear Modulus μ_1 GPa	Transient Shear Modulus μ_2 GPa
M1*	2.8×10^{18}	1.0×10^{17}	2.0×10^{19}	70	70
M2†	7.7×10^{18}	1.7×10^{17}	7.7×10^{18}	70	70
M3‡	2.8×10^{18}	∞	2.0×10^{19}	70	—

* Constrained such that lower crust viscosity $\eta_c = 7 \times \eta_1$ and $\mu_2 = \mu_1$

† Constrained such that lower crust viscosity $\eta_c = 1 \times \eta_1$ and $\mu_2 = \mu_1$

‡ Constrained such that lower crust viscosity $\eta_c = 7 \times \eta_1$ and $\eta_2 = \infty$

Figure 1

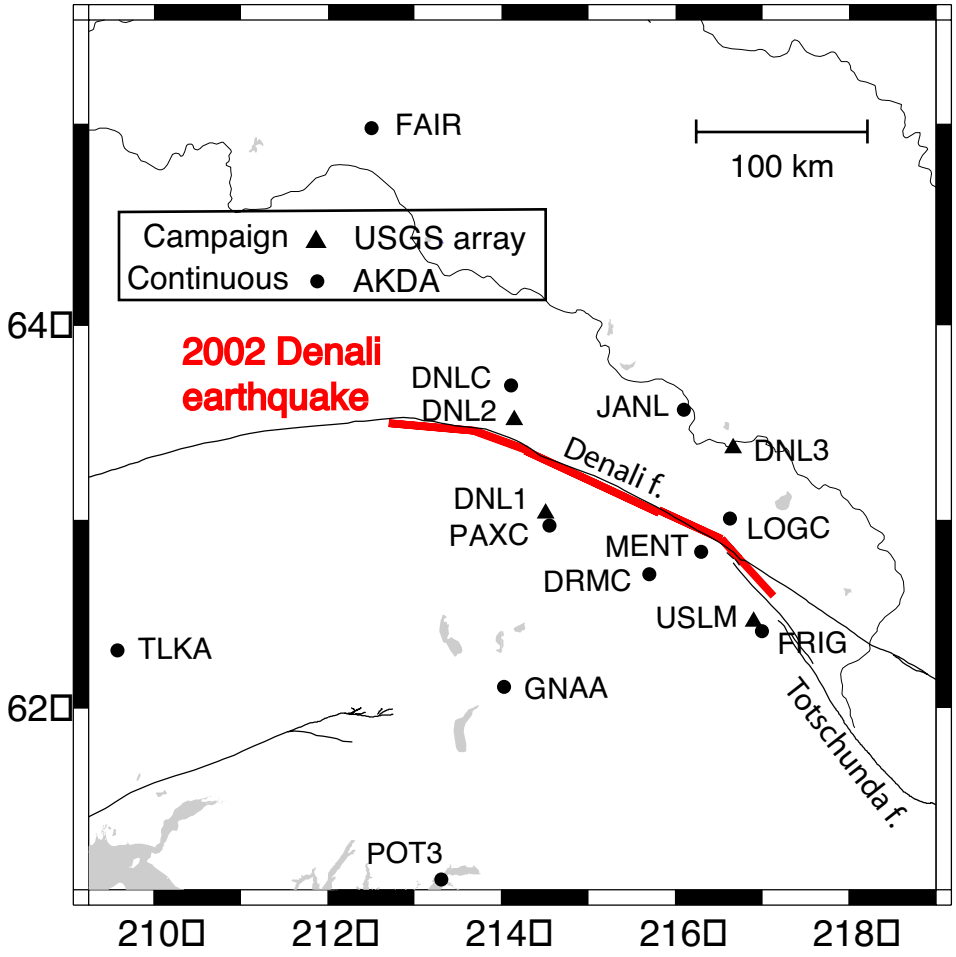
FAIR
100 km
Campaign ▲ USGS array
Continuous ● AKDA
64
2002 Denali
earthquake
DNLC
DNL2
JANL
DNL3
Denali f.
DNL1
PAXC
LOGC
MENT
DRMC
USLM
FRIG
TLKA
GNAA
Totschunda f.
POT3
62
210
212
214
216
218

Figure 2

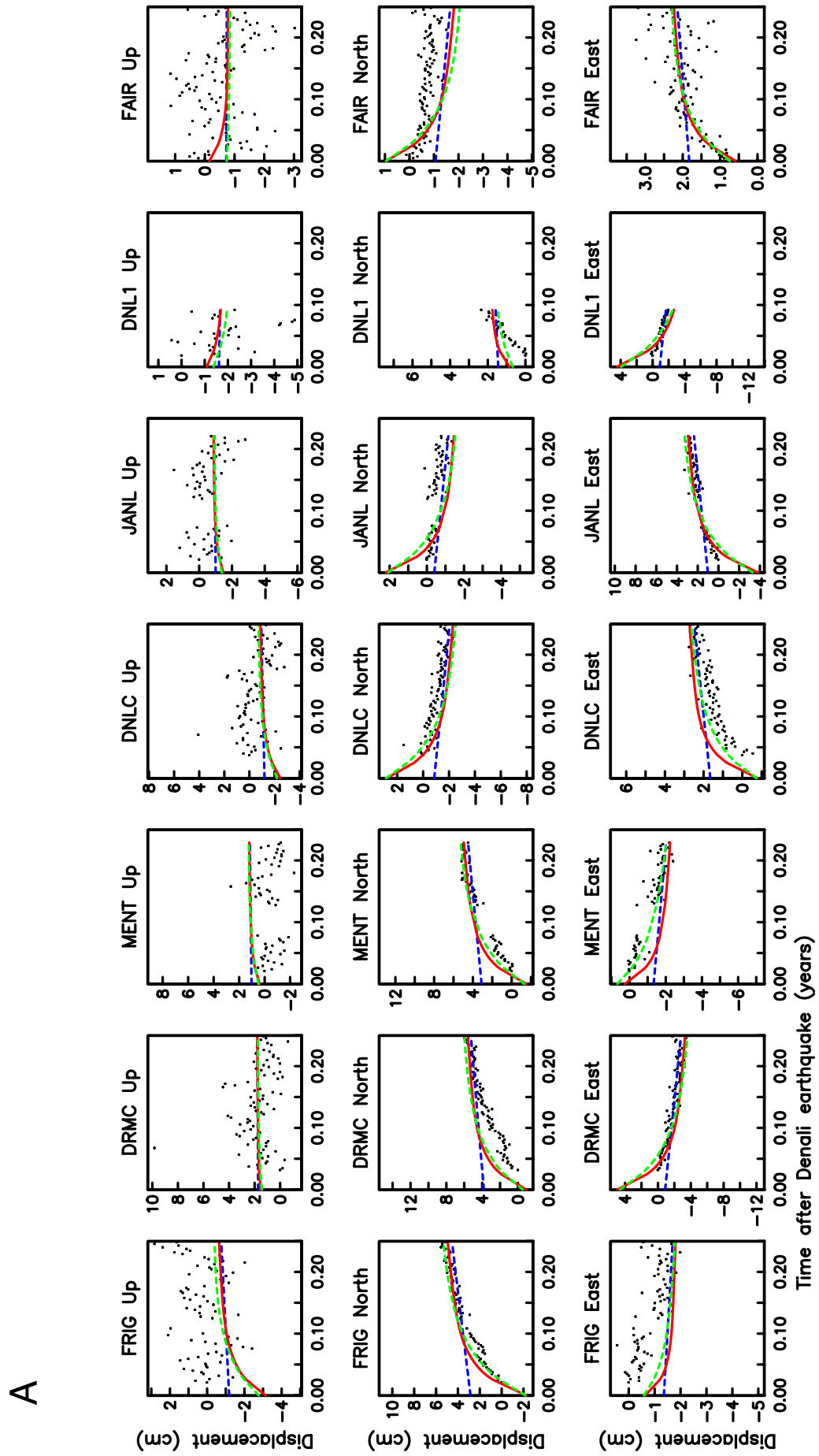
A
FRIG Up
DRMC Up
MENT Up
DNLC Up
JANL Up
DNL1 Up
FAIR Up
FRIG North
DRMC North
MENT North
DNLC North
JANL North
DNL1 North
FAIR North
FRIG East
DRMC East
MENT East
DNLC East
JANL East
DNL1 East
FAIR East
Displacement (cm)
Time after Denali earthquake (years)

Figure 2

B

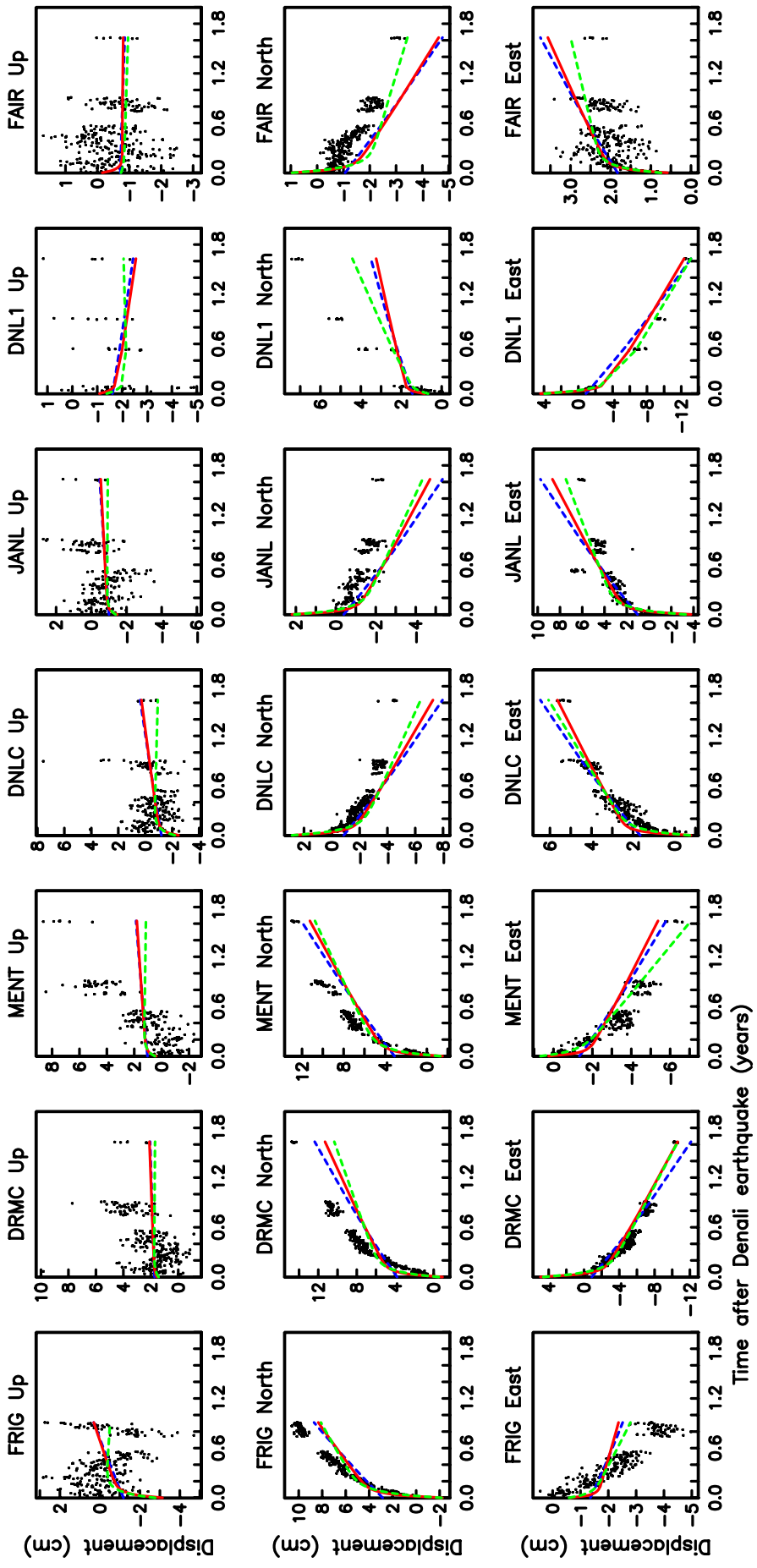
FRIG Up
DRMC Up
MENT Up
DNLC Up
JANL Up
DNL1 Up
FAIR Up
FRIG North
DRMC North
MENT North
DNLC North
JANL North
DNL1 North
FAIR North
FRIG East
DRMC East
MENT East
DNLC East
JANL East
DNL1 East
FAIR East
Displacement (cm)
Time after Denali earthquake (years)

Figure 2

C

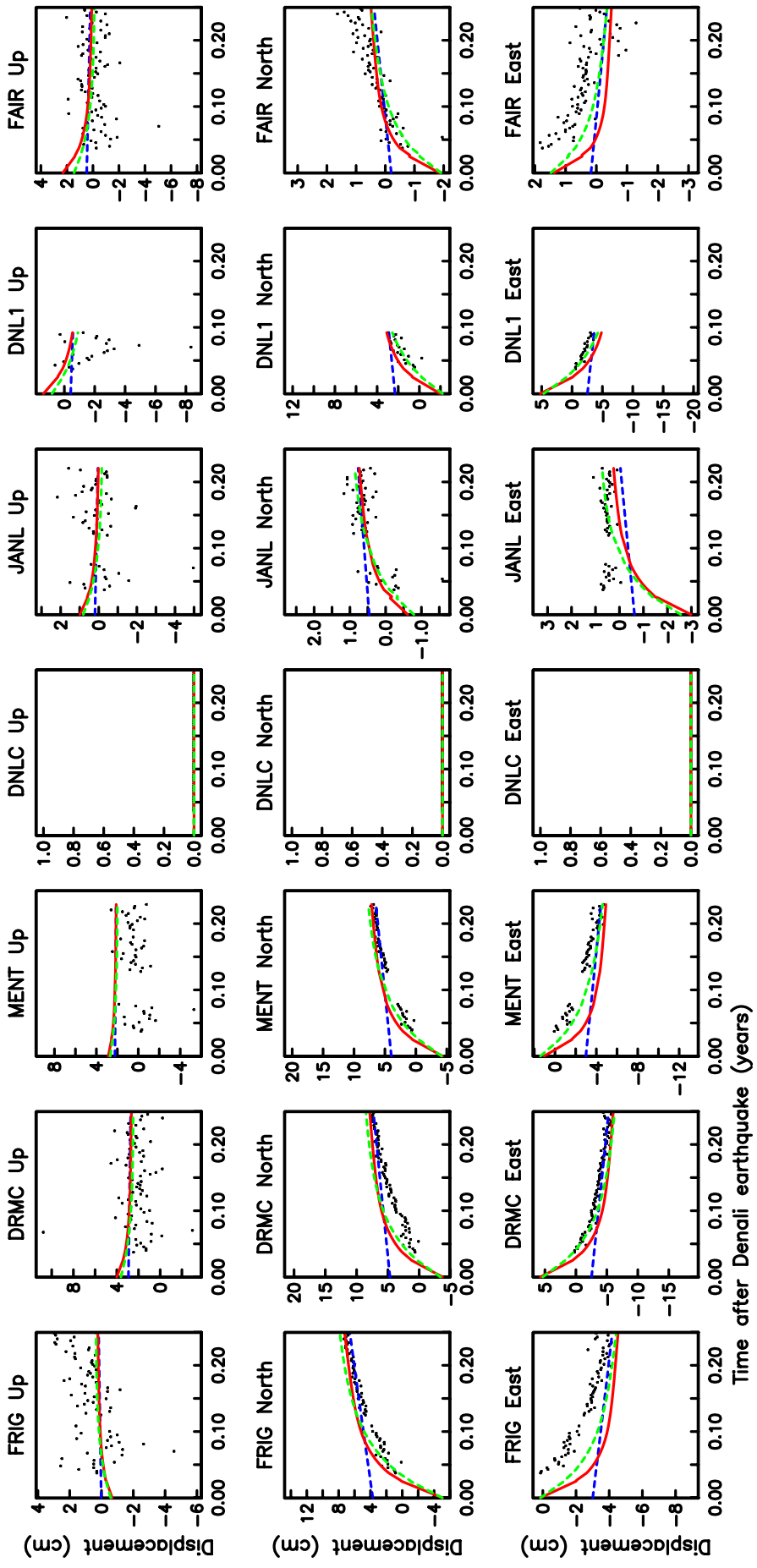
FRIG Up
DRMC Up
MENT Up
DNLC Up
JANL Up
DNL1 Up
FAIR Up
FRIG North
DRMC North
MENT North
DNLC North
JANL North
DNL1 North
FAIR North
FRIG East
DRMC East
MENT East
DNLC East
JANL East
DNL1 East
FAIR East
Displacement (cm)
Time after Denali earthquake (years)

Figure 2

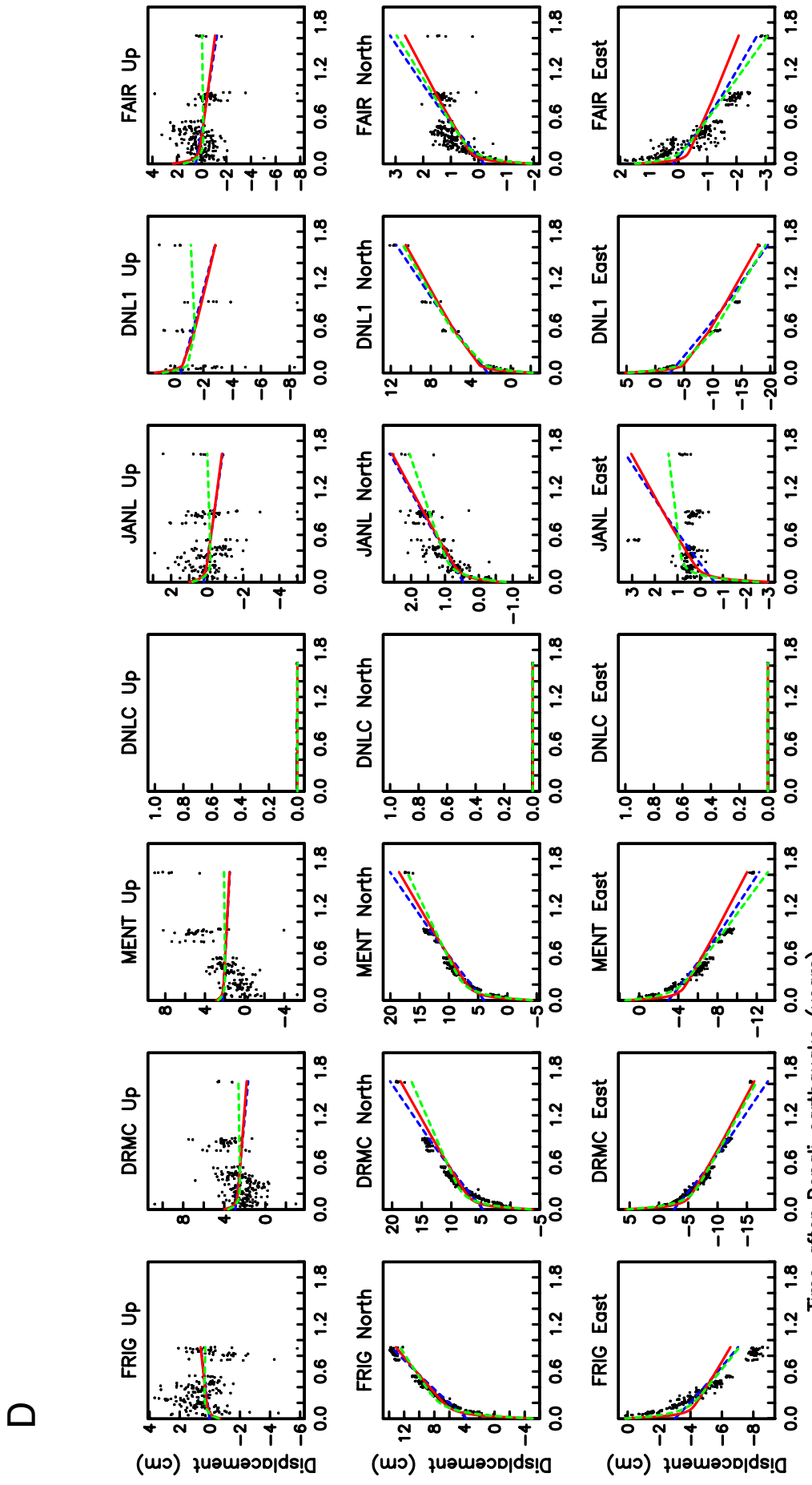
D
FRIG Up
DRMC Up
MENT Up
DNLC Up
JANL Up
DNL1 Up
FAIR Up
FRIG North
DRMC North
MENT North
DNLC North
JANL North
DNL1 North
FAIR North
FRIG East
DRMC East
MENT East
DNLC East
JANL East
DNL1 East
FAIR East
Displacement (cm)
Time after Denali earthquake (years)

Figure 3

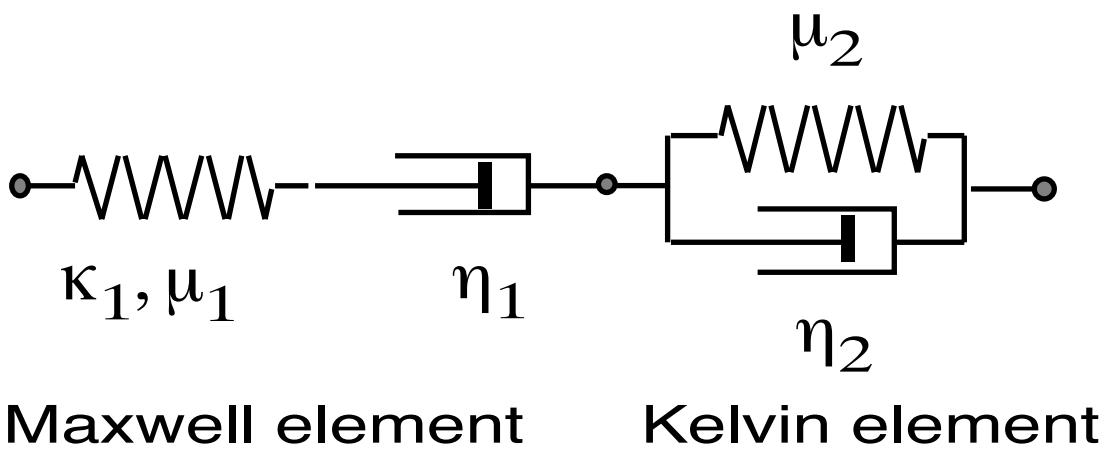

Figure 4

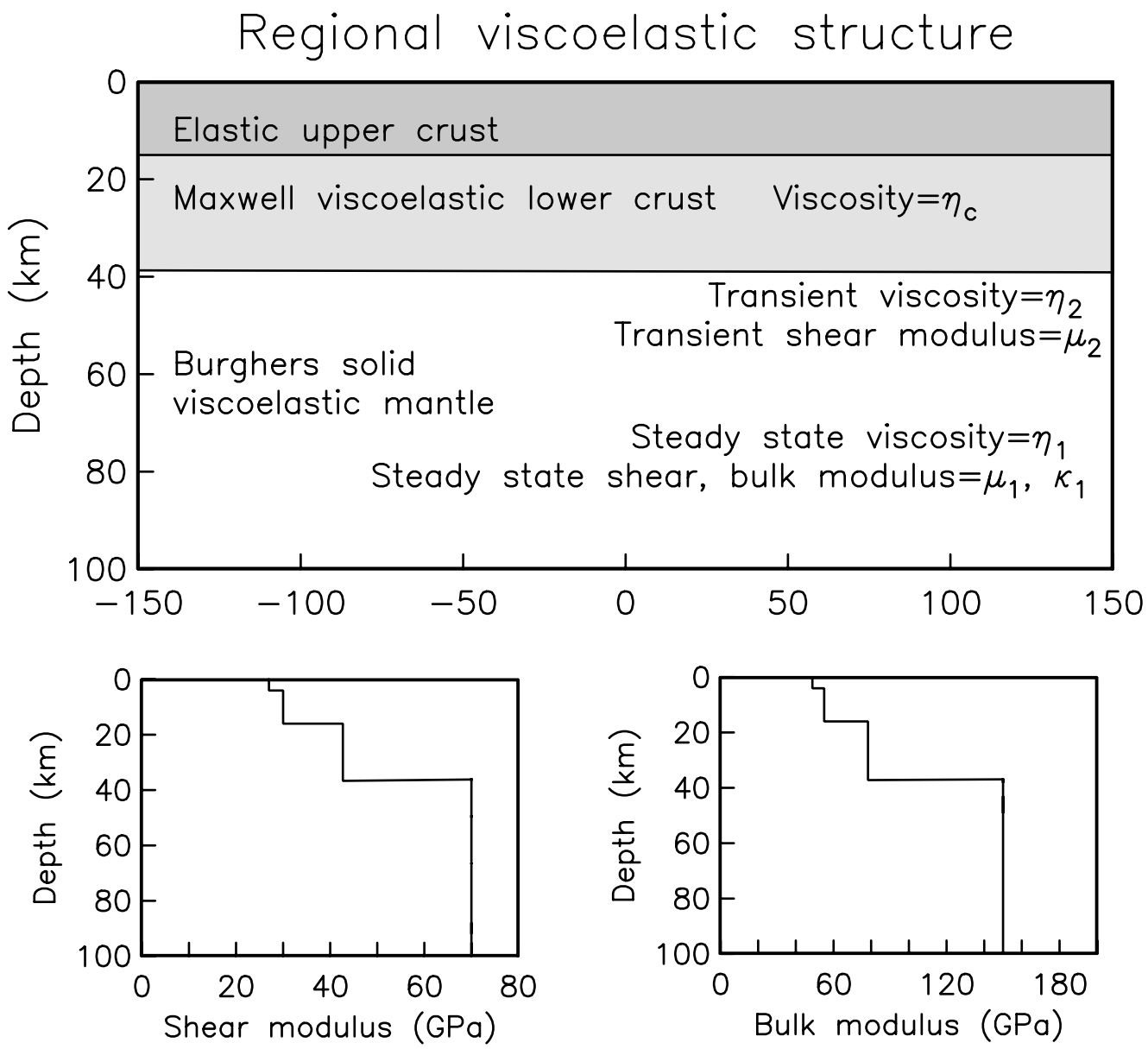
Regional viscoelastic structure
Elastic upper crust
Maxwell viscoelastic lower crust
Viscosity=η_c
Transient viscosity=η_2
Transient shear modulus=μ_2
Burghers solid
viscoelastic mantle
Steady state viscosity=η_1
Steady state shear, bulk modulus=μ_1, κ_1
Depth (km)
0
20
40
60
80
100
−150
−100
−50
0
50
100
150
Depth (km)
Shear modulus (GPa)
0
20
40
60
80
Depth (km)
Bulk modulus (GPa)
0
60
120
180

Figure 5

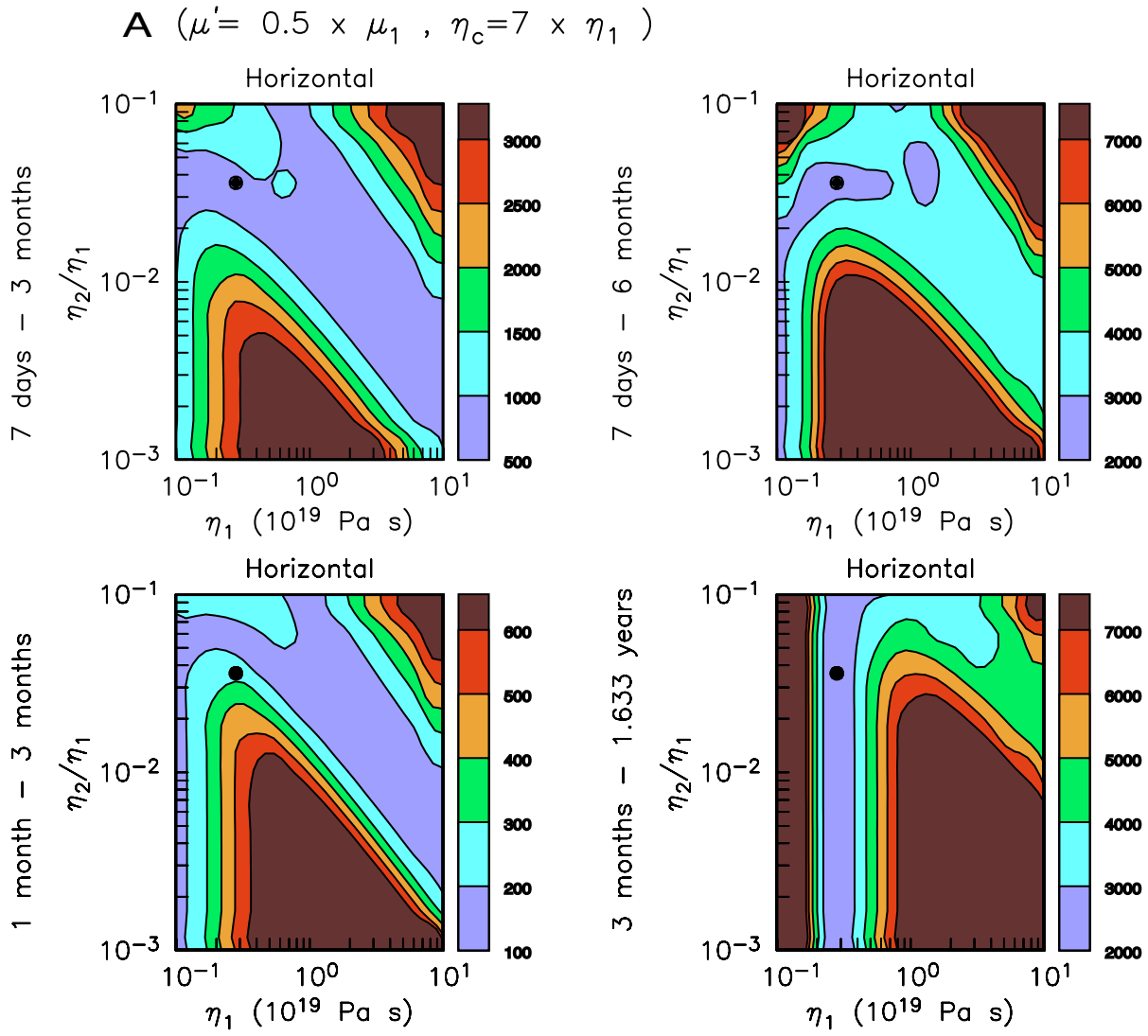
A (μ'= 0.5 x μ_1 , η_c=7 x η_1)
Horizontal
7 days – 3 months
7 days – 6 months
1 month – 3 months
3 months – 1.633 years
η_2/η_1
η_1 (10^{19} Pa s)
10^{-1}
10^{-2}
10^{-3}
10^{0}
10^{1}
3000
2500
2000
1500
1000
500
7000
6000
5000
4000
600
400
300
200
100

Figure 5

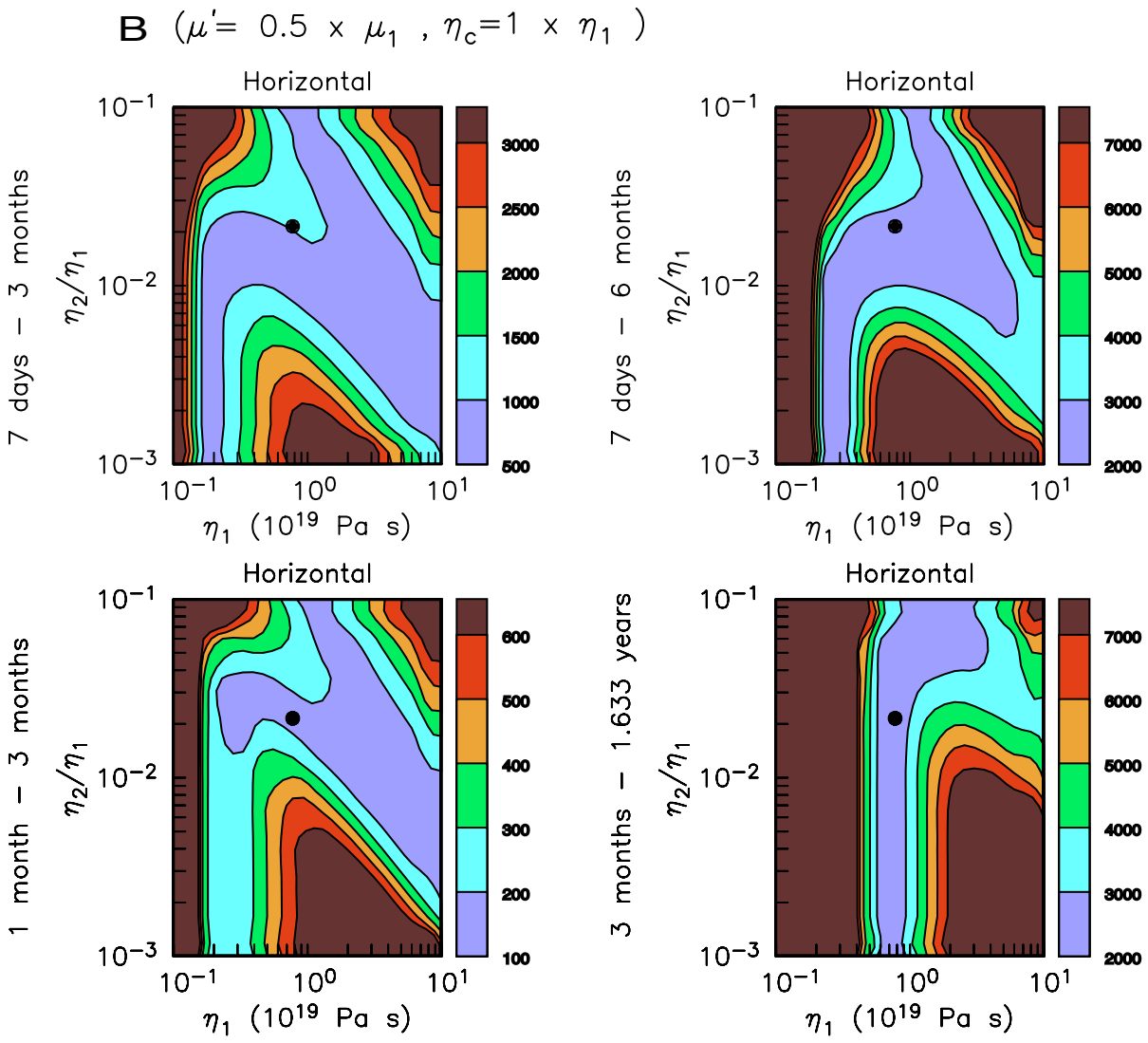
B (μ'= 0.5 x μ_1 , η_c=1 x η_1)
Horizontal
7 days – 3 months
η_2/η_1
10^{-1}
10^{-2}
10^{-3}
10^{-1}
10^{0}
10^{1}
η_1 (10^{19} Pa s)
3000
2500
2000
1500
1000
500
Horizontal
7 days – 6 months
η_2/η_1
10^{-1}
10^{-2}
10^{-3}
10^{-1}
10^{0}
10^{1}
η_1 (10^{19} Pa s)
7000
6000
5000
4000
3000
2000
Horizontal
1 month – 3 months
η_2/η_1
10^{-1}
10^{-2}
10^{-3}
10^{-1}
10^{0}
10^{1}
η_1 (10^{19} Pa s)
600
500
400
300
200
100
Horizontal
3 months – 1.633 years
η_2/η_1
10^{-1}
10^{-2}
10^{-3}
10^{-1}
10^{0}
10^{1}
η_1 (10^{19} Pa s)
7000
6000
5000
4000
3000
2000

Figure 6

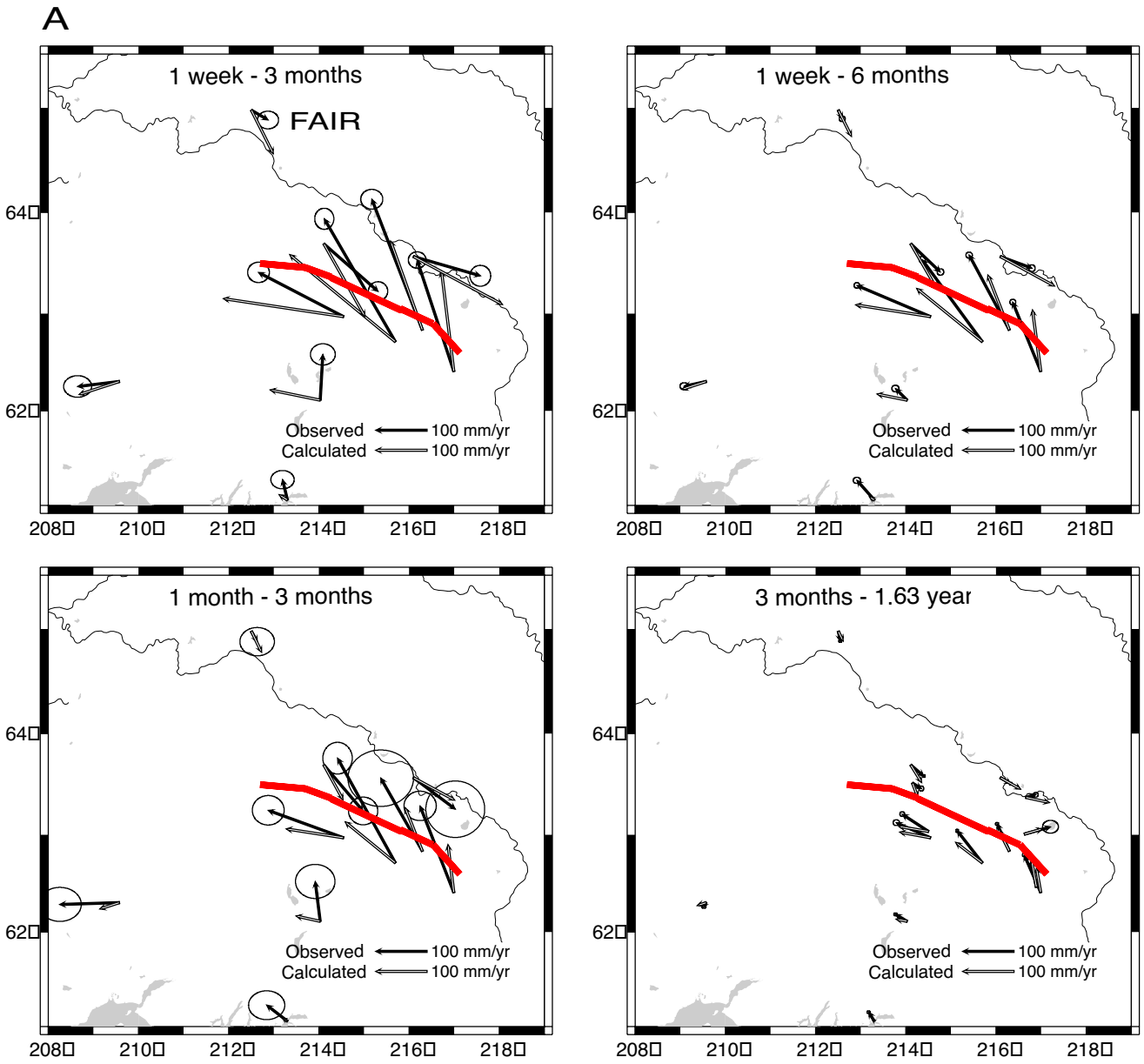
A
1 week - 3 months
FAIR
1 week - 6 months
1 month - 3 months
3 months - 1.63 year
Observed 100 mm/yr
Calculated 100 mm/yr
64
62
208
210
212
214
216
218

Figure 6

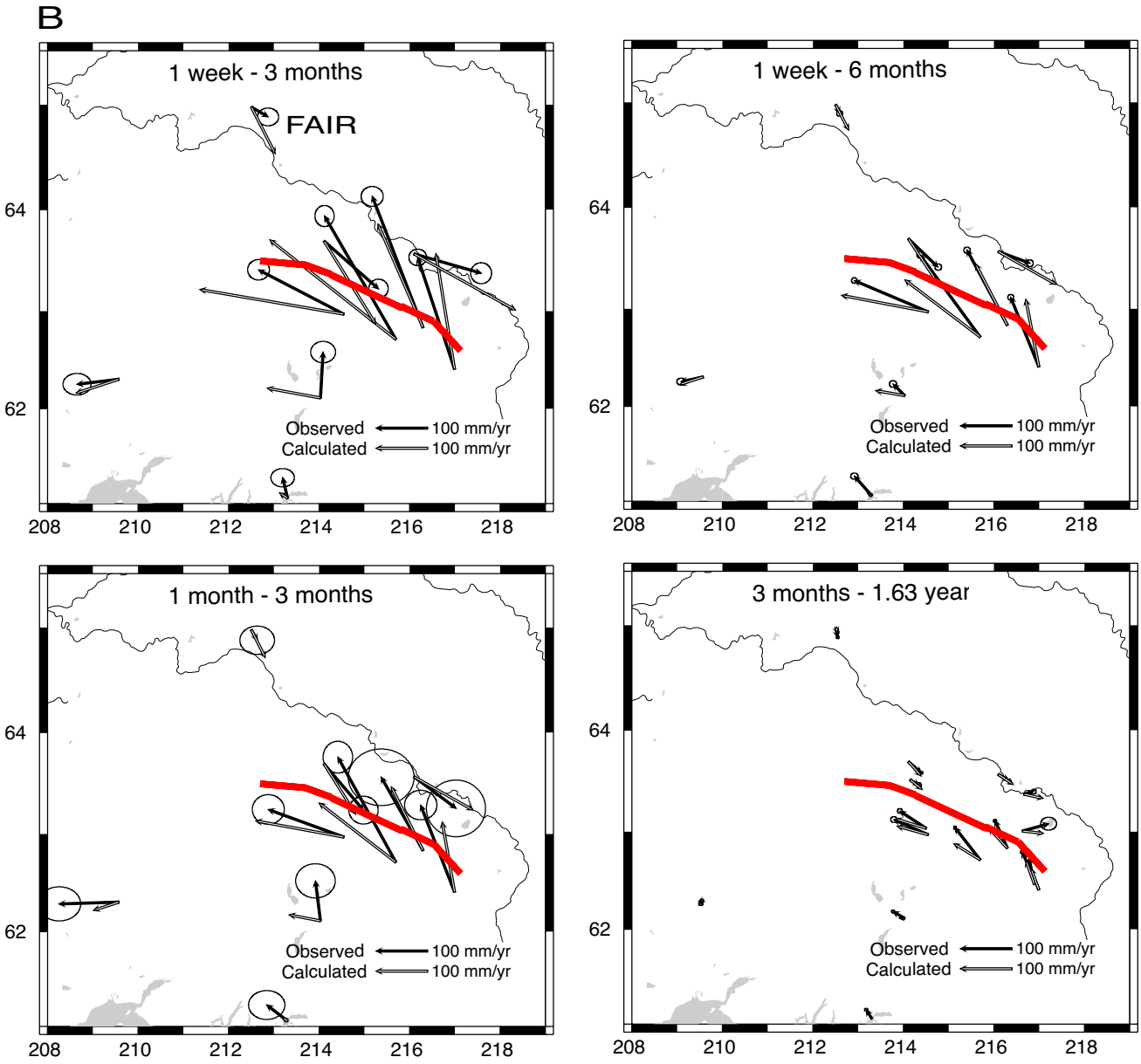
B
1 week - 3 months
FAIR
1 week - 6 months
1 month - 3 months
3 months - 1.63 year
Observed 100 mm/yr
Calculated 100 mm/yr
64
62
208
210
212
214
216
218

Figure 6

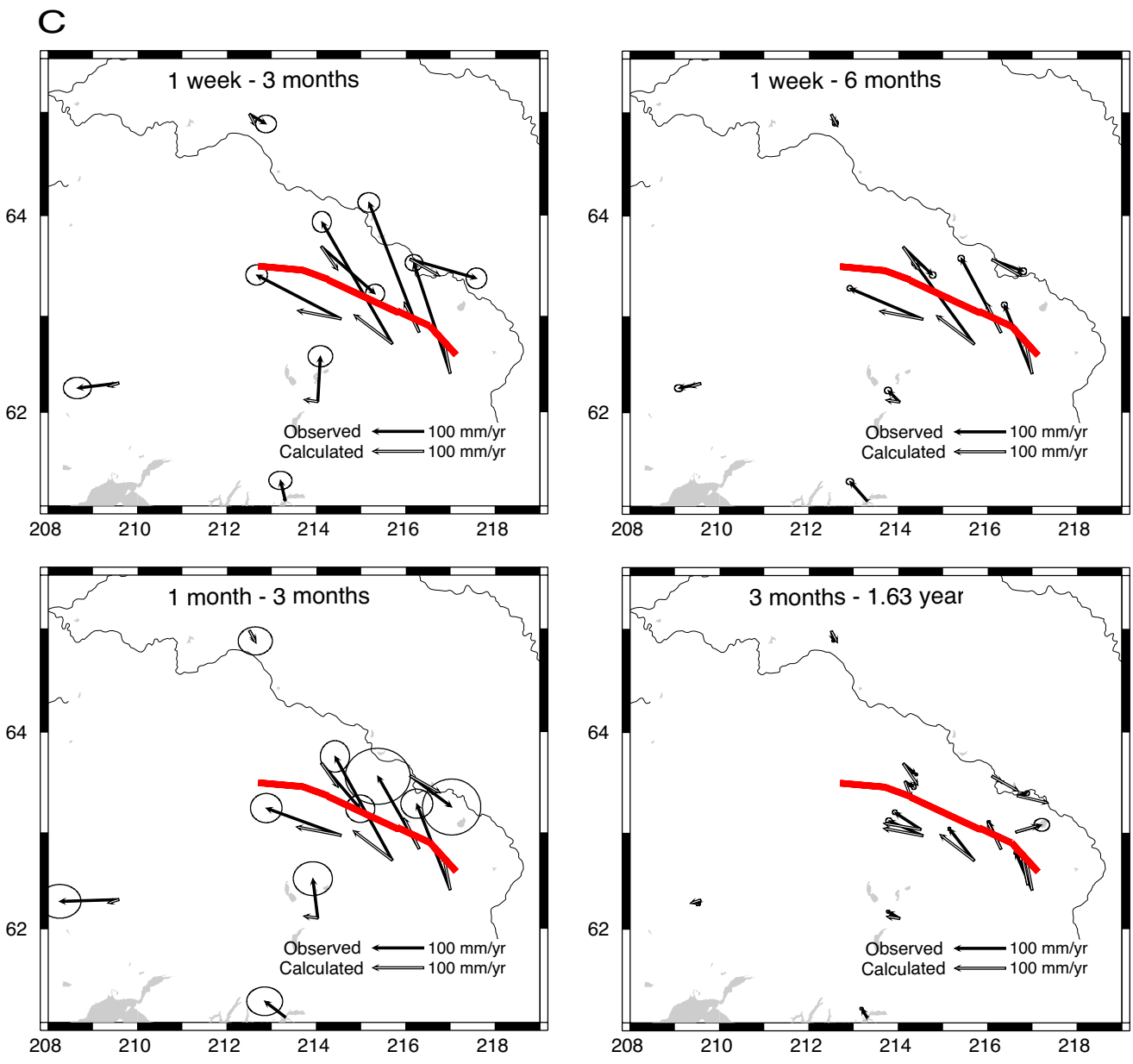
C
1 week - 3 months
1 week - 6 months
1 month - 3 months
3 months - 1.63 year
Observed 100 mm/yr
Calculated 100 mm/yr
64
62
208
210
212
214
216
218

Figure 6

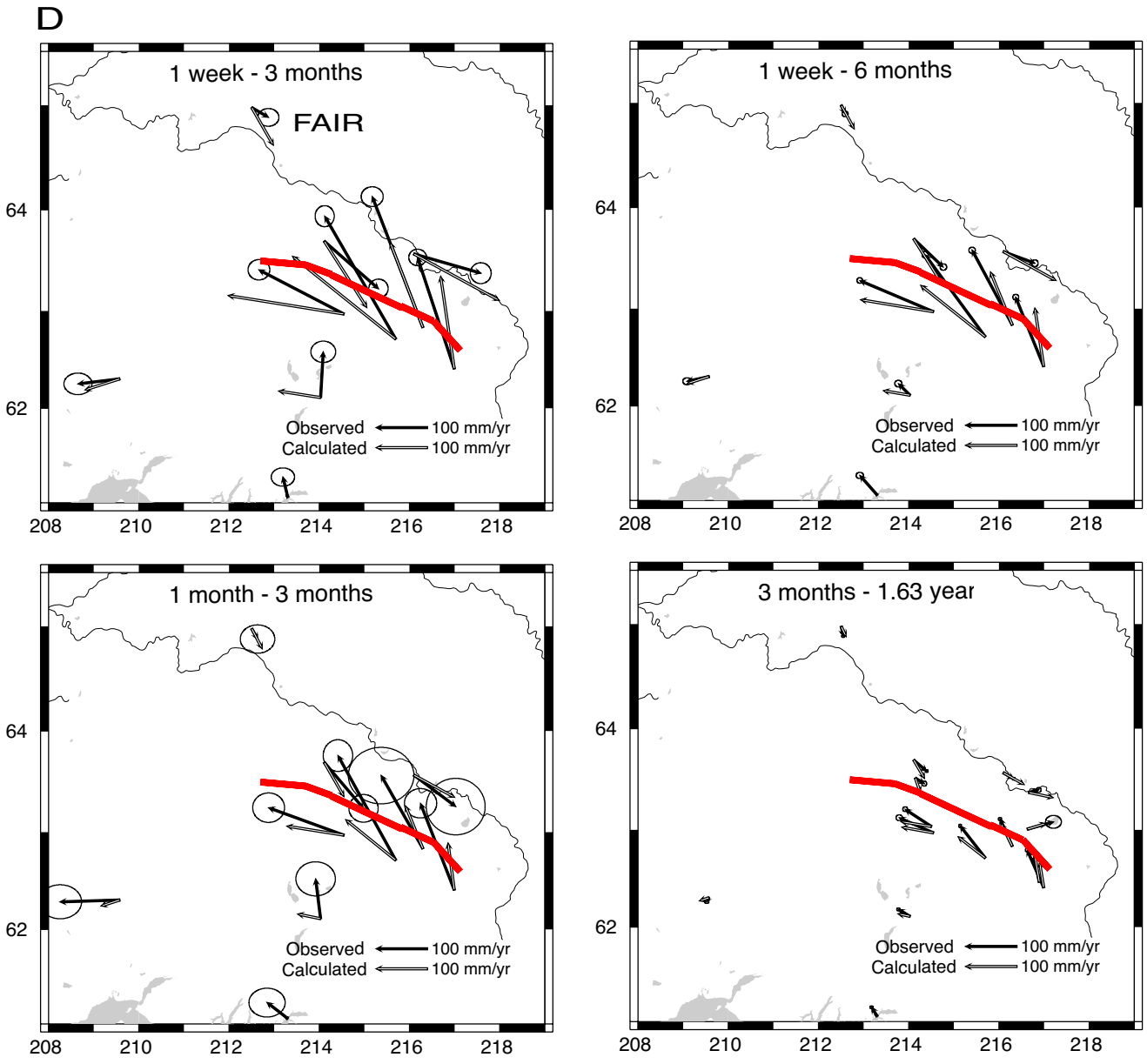
D
1 week - 3 months
FAIR
1 week - 6 months
1 month - 3 months
3 months - 1.63 year
Observed 100 mm/yr
Calculated 100 mm/yr
64
62
208
210
212
214
216
218

Figure 7

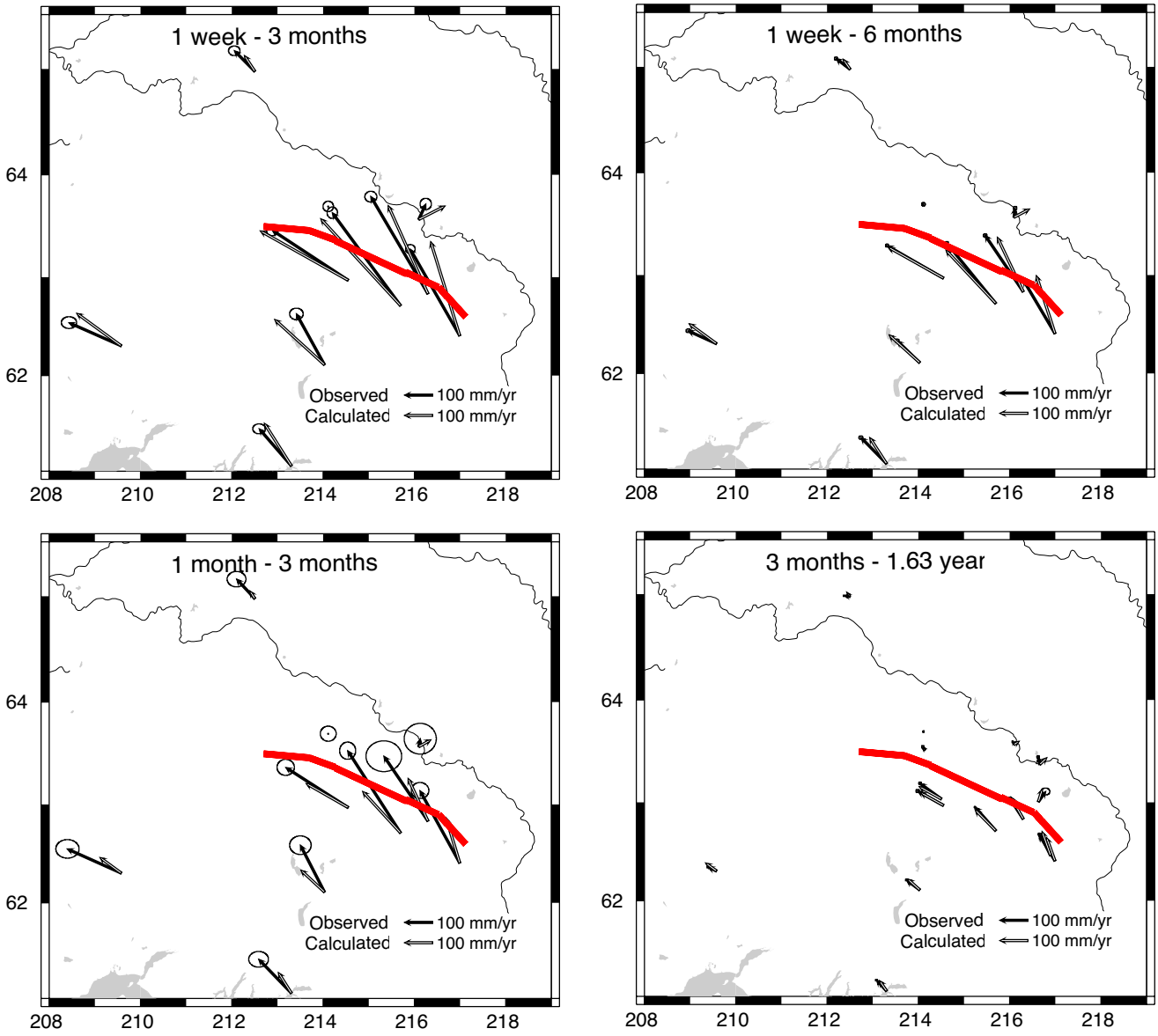
1 week - 3 months
1 week - 6 months
1 month - 3 months
3 months - 1.63 year
Observed 100 mm/yr
Calculated 100 mm/yr
64
62
208
210
212
214
216
218